Supplementary information for "Data-driven quasi-conformal morphodynamic flows"

Salem Mosleh, Gary P. T. Choi, L. Mahadevan

Supplementary text

S1 Computing the shear rate $\mathcal{S}(\mathbf{z}, t)$

In this section, we provide steps to calculate the shear rate, as defined in Eq. (2.14) of the main text. In particular,

$$\mathcal{S}^2(\mathbf{z}, t) \equiv \frac{1}{2}\underline{\dot{g}}^i_j(\mathbf{z}, t)\underline{\dot{g}}^j_i(\mathbf{z}, t), \tag{S1}$$

where $\underline{\dot{g}}^i_j(\mathbf{z}, t)$ is the traceless part of the metric (multiplied by the inverse metric given in Eq. (2.5) in the main text), which is given by

$$\underline{\dot{g}}^i_j(\mathbf{z}, t) \equiv g^{ik}(\mathbf{z}, t)\left[\dot{g}_{kj}(\mathbf{z}, t) - \frac{1}{2}\dot{g}^\ell_\ell(\mathbf{z}, t)g_{kj}(\mathbf{z}, t)\right] \tag{S2}$$

where repeated indices are summed over and indices are raised by multiplication with the inverse metric. To evaluate this expression and derive Eq. (2.15) in the main text, we use Eqs. (2.5 & 2.10) in the main text to get

$$\dot{g}^i_j = g^{ik}\dot{g}_{kj} = \frac{\dot{\omega}}{\omega}\,\delta^i_j + \mathbf{J}^i_\top \mathbf{R}^\top \mathbf{E}^{-1}\mathbf{R}\mathbf{J}^k\left(\frac{\dot{K}}{K}\mathbf{J}^\top_k\,\mathbf{R}^\top\,\mathbf{E}\,\sigma_Z\,\mathbf{R}\,\mathbf{J}_j + \dot{\theta}\mathbf{J}^\top_k\left[\Sigma_2, \mathbf{R}^\top\,\mathbf{E}\,\mathbf{R}\right]\mathbf{J}_j\right), \tag{S3}$$

where here, and in the following expressions, we suppress the dependence on $(\mathbf{z}, t)$ for simplicity. To evaluate Eq. (S1), we will use the following properties of the Jacobian and Levi-Civita symbol, namely,

$$\mathbf{J}^i_\top(\mathbf{z})\mathbf{J}_j(\mathbf{z}) = \delta_{ij}, \qquad \mathbf{J}^i(\mathbf{z})\mathbf{J}^\top_i(\mathbf{z}) = \mathbf{I}_2, \quad \text{and} \quad R^\top(\mathbf{z}, t)\Sigma_2 R(\mathbf{z}, t) = \Sigma_2. \tag{S4}$$

Using these properties, Eq. (S3) simplifies to

$$\dot{g}^i_j = \frac{\dot{\omega}}{\omega}\,\delta^i_j + \frac{\dot{\epsilon}}{1+\epsilon}\mathbf{J}^i_\top\mathbf{R}^\top\sigma_Z\,\mathbf{R}\,\mathbf{J}_j + \dot{\theta}\mathbf{J}^i_\top\mathbf{R}^\top\left(\mathbf{E}^{-1}\Sigma_2\mathbf{E} - \Sigma_2\right)\,\mathbf{R}\,\mathbf{J}_j \tag{S5}$$

and, using the cyclical property of the trace, we get

$$\mathcal{D} = \frac{1}{2}\dot{g}^i_i = \frac{\dot{\omega}}{\omega} + \frac{1}{2}\frac{\dot{K}}{K}Tr\left[\sigma_Z\right] + \frac{\dot{\theta}}{2}Tr\left[\mathbf{E}^{-1}\Sigma_2\mathbf{E} - \Sigma_2\right] = \frac{\dot{\omega}}{\omega}, \tag{S6}$$

as given in Eq. (2.13) in the main text, where we used the fact that the Pauli matrices σ_Z and $\Sigma_2 = i\sigma_Y$ have zero trace. Thus, we have

$$\underline{\dot{g}}^i_j = \mathbf{J}^i_\top\mathbf{R}^\top\left[\frac{\dot{K}}{K}\sigma_Z + \dot{\theta}\left(\mathbf{E}^{-1}\Sigma_2\mathbf{E} - \Sigma_2\right)\right]\,\mathbf{R}\,\mathbf{J}_j. \tag{S7}$$

Now we can evaluate the shear rate as (using the properties of the trace and Jacobian again),

$$\mathcal{S}^2 \equiv \frac{1}{2}\underline{\dot{g}}^i_j\underline{\dot{g}}^j_i = \frac{1}{2}Tr\left[\left(\frac{\dot{K}}{K}\sigma_Z + \dot{\theta}\left(\mathbf{E}^{-1}\Sigma_2\mathbf{E} - \Sigma_2\right)\right)^2\right]. \tag{S8}$$

Using the properties of the Pauli matrices, we have $Tr[\sigma_Z^2] = 2$, $Tr[\Sigma_2^2] = -Tr[\sigma_Y^2] = -2$, and $Tr[\sigma_Z\Sigma_2] = 0$, and the fact that both $\mathbf{E}$ and σ_Z are diagonal matrices (and therefore commute), we get

$$\mathcal{S}^2 = \left(\frac{\dot{K}}{K}\right)^2 - 2\dot{\theta}^2 - \dot{\theta}^2 Tr[\mathbf{E}^{-1}\Sigma_2\mathbf{E}\Sigma_2]. \tag{S9}$$

We can explicitly calculate the trace in the last term using the definitions of the Levi-Civita symbol and $\mathbf{E}$ given in Eq. (2.3) of the main text to get,

$$Tr[\mathbf{E}^{-1}\Sigma_2\mathbf{E}\Sigma_2] = -\frac{1}{K^2(\mathbf{z},t)} - K^2(\mathbf{z},t). \tag{S10}$$

Finally, after plugging this back into Eq. (S9), we can simplify the answer to

$$\mathcal{S}^2(\mathbf{z},t) = \left(\frac{\dot{K}(\mathbf{z},t)}{K(\mathbf{z},t)}\right)^2 + \frac{\left[K^2(\mathbf{z},t)-1\right]^2\ \dot{\theta}^2(\mathbf{z},t)}{K^2(\mathbf{z},t)}, \tag{S11}$$

As given in Eq. (2.14) in the main text.

We end this section by illustrating the use of Eq. (S11) to connect $k-$quasi-conformal flows with $K-$quasi-conformal maps. Writing Eq. (S11) as

$$\mathcal{S}^2(\mathbf{z},t) = \left(\frac{d}{dt}\ln K(\mathbf{z},t)\right)^2 + \frac{\left[K^2(\mathbf{z},t)-1\right]^2\ \dot{\theta}^2(\mathbf{z},t)}{K^2(\mathbf{z},t)}. \tag{S12}$$

and noting that all the terms in this equation are positive, we have that

$$k \geq \mathcal{S}(\mathbf{z},t) \geq \left|\frac{d}{dt}\ln K(\mathbf{z},t)\right| \implies K(\mathbf{z},t) \leq e^{kt}. \tag{S13}$$

This last result is consistent with the result in Ref. [1].

S2 Discretizing the strain-rate tensor $\mathbf{G}(f_M, t_N)$

In this section, we provide supporting derivations and explicit examples in the computation of the growth strain tensor $\mathbf{G}(\mathbf{z},t)$ defined in Eq. (2.17) and discretised in Eq. (3.10) the main text. Since the computation of the viscous cost, Eqs. (2.18 & 3.17) in the main text, is done separately for each triangle and each time point, we will demonstrate the calculations using a single triangle at time t_N. Without loss of generality (up to a rotation and scaling), we can orient and scale our global coordinate system so that the initial triangle is:

$$\mathbf{P}_0(t_N) = \mathbf{0}, \qquad \mathbf{P}_1(t_N) = \hat{x}, \quad \text{and} \quad \mathbf{P}_2(t_N) = x(t_N)\hat{x} + y(t_N)\hat{y}, \tag{S14}$$

where $y \neq 0$ so that the triangle is not degenerate. In other words, we align one edge with the $x-$axis, the plane of the triangle along the $z-$axis, and rescale the triangle so that the edge has unit length. This is only done to simplify the example calculations in this section. The edges of this triangle are

$$\mathbf{E}_1(t_N) = \hat{x} \qquad \text{and} \qquad \mathbf{E}_2(t_N) = x(t_N)\hat{x} + y(t_N)\hat{y}. \tag{S15}$$

We can use these edges to define a convenient coordinate system on the triangle that helps us approximate the quantities defined on the smooth $\mathbf{X}(\mathbf{z}, t)$ using the triangulation. In particular, we parametrize a point on the triangle using (barycentric coordinates),

$$\mathbf{X}(\mathbf{z}, t_N) = \mathbf{P}_0(t_N) + z_1\mathbf{E}_1(t_N) + z_2\mathbf{E}_2(t_N), \qquad z_1 + z_2 \leq 1, \tag{S16}$$

and $0 \leq z_1, z_2 \leq 1$. For example, in the right triangle described by Eq. (S14) with $x(t_N) = 0, y(t_N) = 1$, the coordinates (z_1, z_2) are simply the Cartesian coordinates on the $xy-$plane and the range $z_1 + z_2 \leq 1$ spans the triangle. Using Eq. (S16), we can calculate the metric defined in Eq. (2.1) of the main text, which will be constant on the triangle and given by

$$\partial_i\mathbf{X}(\mathbf{z}, t_N) = \mathbf{E}_i(t_N), \quad g_{ij}(t_N) = \mathbf{E}_i(t_N)\cdot\mathbf{E}_j(t_N) = \begin{pmatrix} 1 & x(t_N) \\ x(t_N) & x^2(t_N) + y^2(t_N) \end{pmatrix}, \tag{S17}$$

where the second equality follows for the specific triangle Eq. (S14). When $x(t_N) = 0, y(t_N) = 1$, this reduces to the identity matrix as expected. Using the determinant of the metric, which is equal to $g(t_N) = y^2(t_N)$, we can find the area of the triangle as

$$\mathcal{A}_N \equiv \int_{z_1=0}^{1}\int_{z_2=0}^{1-z_1}\sqrt{g(t_N)}dz_1dz_2 = \frac{\sqrt{g(t_N)}}{2} = \frac{y(t_N)}{2}. \tag{S18}$$

The inverse metric Eq. (S17) is

$$g^{ij}(t_N) = \begin{pmatrix} 1 + \frac{x^2(t_N)}{y^2(t_N)} & -\frac{x(t_N)}{y^2(t_N)} \\ -\frac{x(t_N)}{y^2(t_N)} & \frac{1}{y^2(t_N)} \end{pmatrix}, \tag{S19}$$

which can be used to calculate the dual basis defined as

$$\partial^i\mathbf{X}(\mathbf{z}, t_N) \equiv g^{ik}(t_N)\partial_k\mathbf{X}(\mathbf{z}, t_N) = \mathbf{E}^k(t_N), \tag{S20}$$

$$\mathbf{E}^1(t_N) = g^{11}(t_N)\mathbf{E}_1(t_N) + g^{12}(t_N)\mathbf{E}_2(t_N) = \hat{x} - \frac{x(t_N)}{y(t_N)}\hat{y}, \quad \mathbf{E}^2(t_N) = \frac{\hat{y}}{y(t_N)}. \tag{S21}$$

Note that it is straightforward to check the properties of the dual basis given in Eq. (3.6) of the main text. In particular, $\mathbf{E}^i(t_N)\cdot\mathbf{E}_j(t_N) = \delta^i_j$ and

$$\mathbf{Q}_{\|}(t_N) \equiv \mathbf{E}_1(t_N)\otimes\mathbf{E}^1(t_N) + \mathbf{E}_2(t_N)\otimes\mathbf{E}^2(t_N) = \begin{pmatrix} 1 & 0 & 0 \\ 0 & 1 & 0 \\ 0 & 0 & 0 \end{pmatrix}, \tag{S22}$$

which is the projection operator onto the plane of the triangle in the embedding space $\mathbb{R}^3$, which will be the case for any triangle. In calculating this we wrote, for example, $\hat{x} = (1, 0, 0)^\top$, $\hat{y} = (0, 1, 0)^\top$, and

$$\hat{x}\otimes\hat{y} = \begin{pmatrix} 1 \\ 0 \\ 0 \end{pmatrix}\begin{pmatrix} 0 & 1 & 0 \end{pmatrix} = \begin{pmatrix} 0 & 1 & 0 \\ 0 & 0 & 0 \\ 0 & 0 & 0 \end{pmatrix}. \tag{S23}$$

Using Eqs. (S16–S17), the factor $\boldsymbol{\mathcal{T}}^{ij}(t_N)$ defined in the second half of Eq. (3.7) in the main text can be written as

$$\boldsymbol{\mathcal{T}}^{ij}(t_N) = \mathbf{E}^i(t_N)\otimes\mathbf{E}^j(t_N), \tag{S24}$$

from which the first half of Eq. (3.7) in the main text readily follows using the definition of the dual basis Eq. (S20). Equation (S24) shows that $\boldsymbol{\mathcal{T}}^{ij}(t_N)$ gives a basis of tensors in $\mathbb{R}^3$, or 3×3 matrices whose null

space is normal to the triangle. The factor $\boldsymbol{\mathcal{T}}^{ij}(t_N)$ can be used to represent tensors, for example $g_{ij}(t_N)$, as 3×3 matrices, as given in Eq. (3.7) in the main text. For example, using Eq. (S17), the strain rate tensor $\dot{g}_{ij}(t_N)$ is given by

$$\dot{g}_{ij}(t_N) = \partial_i \mathbf{X}(\mathbf{z},t_N)\cdot\partial_j \mathbf{V}(\mathbf{z},t_N) + \partial_i \mathbf{V}(\mathbf{z},t_N)\cdot\partial_j \mathbf{X}(\mathbf{z},t_N) = \mathbf{E}_i(t_N)\cdot\dot{\mathbf{E}}_j(t_N) + \dot{\mathbf{E}}_i(t_N)\cdot\mathbf{E}_j(t_N). \quad \text{(S25)}$$

When $x(t_N)=0, y(t_N)=1$, we have

$$\dot{g}^j_i(t_N) = \begin{pmatrix} 0 & \dot{x}(t_N) \\ \dot{x}(t_N) & 2\dot{y}(t_N)\end{pmatrix}, \qquad \mathcal{D}(t_N) = \dot{y}(t_N), \qquad \mathcal{S}(t_N) = \sqrt{2\dot{y}^2(t_N)+\dot{x}^2(t_N)}. \quad \text{(S26)}$$

Here we used the definition of $\mathcal{D}(t_N)$ and $\mathcal{S}(t_N)$ in Eqs. (2.13–2.14) from the main text. Note that since for $x(t_N)=0, y(t_N)=1$, the area of the triangle was $\delta\mathcal{A}_N = y(t_N)/2$, as given in Eq. (S18), the relative change of area is $\mathcal{D}(t_N) = \dot{\mathcal{A}}_N/\mathcal{A}_N$ as expected. Furthermore, setting $\dot{y}(t_N)=0$ gives a simple shear and in that case $\mathcal{D}(t_N)=0$ and $\mathcal{S}(t_N)=|\dot{x}(t_N)|$. We can also calculate these results with the aid of the tensor $\boldsymbol{\mathcal{T}}^{ij}(t_N)$, which facilitates future calculations (especially the spatial gradient as we show in the next section). In particular, assuming $x(t_N)=0, y(t_N)=1$ for illustration,

$$\boldsymbol{\mathcal{J}}(t_N) = \boldsymbol{\mathcal{T}}^{ij}(t_N)\dot{g}_{ij}(t_N) = \begin{pmatrix} 0 & \dot{x}(t_N) & 0 \\ \dot{x}(t_N) & 2\dot{y}(t_N) & 0 \\ 0 & 0 & 0\end{pmatrix}. \quad \text{(S27)}$$

In this case, since the triangle edges are the unit vectors $\hat{x}$ and $\hat{y}$, the matrix $\boldsymbol{\mathcal{J}}(t_N)$ is block diagonal with first 2×2 block being the components $\dot{g}^j_i(t_N)$. In general a rank two tensor and the corresponding 3×3 matrix resulting from multiplication with $\boldsymbol{\mathcal{T}}^{ij}(t_N)$ have the same invariants (traces of products of the matrices or tensors respectively). This follows from properties of the tensor $\boldsymbol{\mathcal{T}}^{ij}(t_N)$, which we give in the next section.

S3 Properties of $\mathcal{T}^{ij}(\mathbf{z},t)$

To compute the invariants of the gradient term we establish the following identities related to the tensor $\mathcal{T}^{ij}$ (note that we may suppress the dependence on $\mathbf{z}$ and t in the following). Its square is given by

$$\boldsymbol{\mathcal{T}}^{ij}\cdot\boldsymbol{\mathcal{T}}^{kl} = \left[\partial^i\mathbf{X}\otimes\partial^j\mathbf{X}\right]\cdot\left[\partial^k\mathbf{X}\otimes\partial^l\mathbf{X}\right] = \left[\partial^i\mathbf{X}\otimes\partial^l\mathbf{X}\right]\partial^i\mathbf{X}\cdot\partial^l\mathbf{X} = \boldsymbol{\mathcal{T}}^{il}g^{jk}, \quad \text{(S28)}$$

while its trace and transpose are given by

$$Tr\left[\boldsymbol{\mathcal{T}}^{ij}\right] = \partial^i\mathbf{X}\cdot\partial^j\mathbf{X} = g^{ij}(\mathbf{z},t), \qquad \boldsymbol{\mathcal{T}}^{ij}_{\top} = \boldsymbol{\mathcal{T}}^{ji}. \quad \text{(S29)}$$

Using these identities we can see how invariants are related, for example

$$Tr[\mathbf{G}(\mathbf{z},t)] = Tr\left[\boldsymbol{\mathcal{T}}^{ij}(\mathbf{z},t)\right]G_{ij}(\mathbf{z},t) = g^{ij}(\mathbf{z},t)G_{ij}(\mathbf{z},t) \quad \text{(S30)}$$

$$Tr[\mathbf{G}^2] = Tr\left[\boldsymbol{\mathcal{T}}^{ij}\boldsymbol{\mathcal{T}}^{kl}\right]G_{ij}G_{kl} = g^{il}g^{kj}G_{ij}G_{kl} = G^j_iG^i_j, \quad \text{(S31)}$$

where we dropped the $(\mathbf{z},t)$ dependence in the second equation. Note that these relations hold for any rank-two tensor, not just $G_{ij}(\mathbf{z},t)$. In addition, we can move between the two representations of the tensors using

$$G_{ij}(\mathbf{z},t) = Tr\left[\boldsymbol{\mathcal{T}}_{ij}\mathbf{G}(\mathbf{z},t)\right]. \quad \text{(S32)}$$

We also define basis matrices related to the normal direction of the surface:

$$\boldsymbol{\mathcal{S}}^i(\mathbf{z},t) \equiv \left[\hat{n}(\mathbf{z},t)\otimes\partial^i\mathbf{X}(\mathbf{z},t)\right], \qquad \boldsymbol{\mathcal{S}}^i_{\top}(\mathbf{z},t) = \left[\partial^i\mathbf{X}(\mathbf{z},t)\otimes\hat{n}(\mathbf{z},t)\right], \quad \text{(S33)}$$

where $\boldsymbol{\mathcal{S}}^i_{\top}$ is the transpose of $\boldsymbol{\mathcal{S}}^i$. Now we have the following additional identities

$$Tr\left[\boldsymbol{\mathcal{S}}^i\right] = 0, \;\; \boldsymbol{\mathcal{S}}^i\cdot\boldsymbol{\mathcal{T}}^{jk} = \boldsymbol{\mathcal{S}}^kg^{ij}, \;\; \boldsymbol{\mathcal{T}}^{jk}\cdot\boldsymbol{\mathcal{S}}^i = 0, \;\; \boldsymbol{\mathcal{S}}^i\cdot\boldsymbol{\mathcal{S}}^j = 0, \;\; \boldsymbol{\mathcal{S}}^i\cdot\boldsymbol{\mathcal{S}}^j_{\top} = g^{ij}\hat{\mathbf{n}}\otimes\hat{\mathbf{n}}, \;\; \boldsymbol{\mathcal{S}}^i_{\top}\cdot\boldsymbol{\mathcal{S}}^j = \boldsymbol{\mathcal{T}}^{ij}. \quad \text{(S34)}$$

S4 Computing the gradient cost

Using the equation

$$\partial_i \partial_j \mathbf{X}(\mathbf{z},t) = \Gamma^k_{ij} \partial_k \mathbf{X}(\mathbf{z},t) + \hat{n}(\mathbf{z},t) b_{ij}(\mathbf{z},t), \tag{S35}$$

and the chain rule, $\nabla_\alpha = \partial_i \mathbf{X}_\alpha \, \partial_i$, it follows that

$$\begin{aligned} \nabla_\alpha \mathbf{G}(\mathbf{z},t) = {} & \partial^i X_\alpha(\mathbf{z},t) \boldsymbol{\mathcal{T}}^{jk}(\mathbf{z},t) \nabla_i G_{jk}(\mathbf{z},t) + \partial^i X_\alpha(\mathbf{z},t) \left[\hat{n}(\mathbf{z},t) \otimes \partial^k \mathbf{X}(\mathbf{z},t)\right] b^j_i(\mathbf{z},t) G_{jk}(\mathbf{z},t) \\ & + \partial^i X_\alpha(\mathbf{z},t) \left[\partial^j \mathbf{X}(\mathbf{z},t) \otimes \hat{n}(\mathbf{z},t)\right] b^k_i(\mathbf{z},t) G_{jk}(\mathbf{z},t). \end{aligned} \tag{S36}$$

Now we can use the identities in Eqs. (S28–S34) to find the invariants of the covariant derivative (square of the trace and trace of the square) given in Eq. (S36). The first invariant we calculate is

$$\sum_{\alpha=1}^{3} Tr\left[\nabla_\alpha \mathbf{G}(\mathbf{z},t)\right] Tr\left[\nabla_\alpha \mathbf{G}(\mathbf{z},t)\right] = \nabla_i G^j_j(\mathbf{z},t) \nabla^i G^k_k(\mathbf{z},t), \tag{S37}$$

while the second is given by

$$\sum_{\alpha=1}^{3} Tr\left[\nabla_\alpha \mathbf{G}(\mathbf{z},t) \cdot \nabla_\alpha \mathbf{G}(\mathbf{z},t)\right] = \nabla_i G_{jk} \nabla^i G^{jk} + 2 b^i_j G^j_k b^k_l G^l_i = \nabla_i G_{jk} \nabla^i G^{jk} + Tr\left[(\mathbf{GB})^2\right]. \tag{S38}$$

In other words, all that is needed to compute the gradient cost term, Eq. (2.20) of the main text is to add the following term proportional to $Tr\left[(\mathbf{GB})^2\right]$ to the expression given in Eq. (3.18) of the main text:

$$\mathcal{C}_{grad} = -B_2 \sum_{M=1}^{M_{max}} \sum_{N=1}^{N_{max}} \delta t_N \, \delta \mathcal{A}_M \;\; Tr\left[\mathbf{G}(f_M,t_N)\mathbf{B}(f_M,t_N)\mathbf{G}(f_M,t_N)\mathbf{B}(f_M,t_N)\right]. \tag{S39}$$

Supplementary figures

Figures S1– S5

Movie captions

Movie S1

Quasi-conformal flows of the *Manduca sexta* (tobacco hawk moth) wing under three different growth models (almost-conformal, viscous, and almost-uniform). The triangles are color-coded according to the normalised dilation rate $\tilde{\mathcal{D}}$, the length of the yellow line segments represents the magnitude of the normalised shear rate $\tilde{\mathcal{S}}$, and their direction is along the largest eigen direction of the strain rate tensor. See Table 2 for the parameter choices of the models.

Movie S2

Quasi-conformal flows of the *Junonia coenia* (buckeye butterfly) wing under three different growth models (almost-conformal, viscous, and almost-uniform).

Movie S3

Quasi-conformal flows of a head mesh evolving towards a sphere under three different growth models (almost-conformal, viscous, and almost-uniform).

Movie S4

Quasi-conformal flows of growing leaves under four different growth models (almost-conformal, viscous, almost-uniform, and geometric).

References

[1] Reimann HM. 1976 Ordinary differential equations and quasiconformal mappings. *Invent. Math.* **33**, 247–270.

[2] Nijhout HF, Cinderella M, Grunert LW. 2014 The development of wing shape in Lepidoptera: mitotic density, not orientation, is the primary determinant of shape. *Evol. Dev.* **16**, 68–77.

[3] Choi GPT, Mahadevan L. 2018 Planar morphometrics using Teichmüller maps. *Proc. R. Soc. A* **474**, 20170905.

[4] Bookstein FL. 1989 Principal warps: Thin-plate splines and the decomposition of deformations. *IEEE Trans. Pattern Anal. Mach. Intell.* **11**, 567–585.

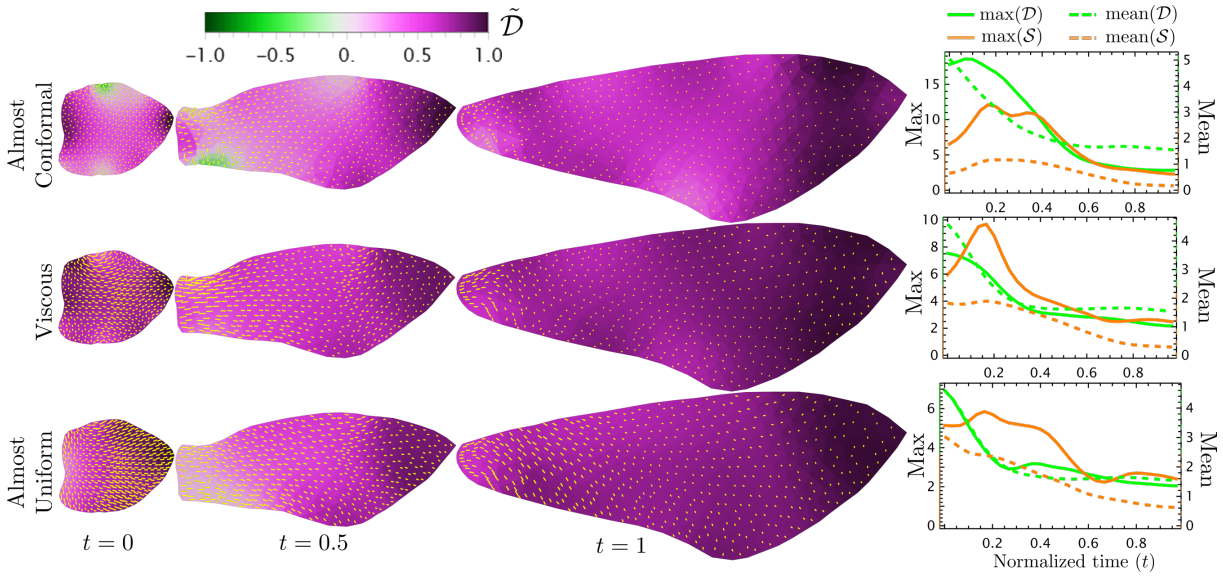

Figure S1: **Optimal 2D quasi-conformal flows for tobacco hawk moth wing registration without landmarks.** Images of growing *Manduca sexta* (tobacco hawk moth) wings are taken from [2] and processed as described in the main text. To infer the possible growth patterns, we run the optimization with three different parameter choices given in Table 2 in the main text: Almost-Conformal, Viscous, and Almost-Uniform (see the caption of main text Fig. 4 for details).

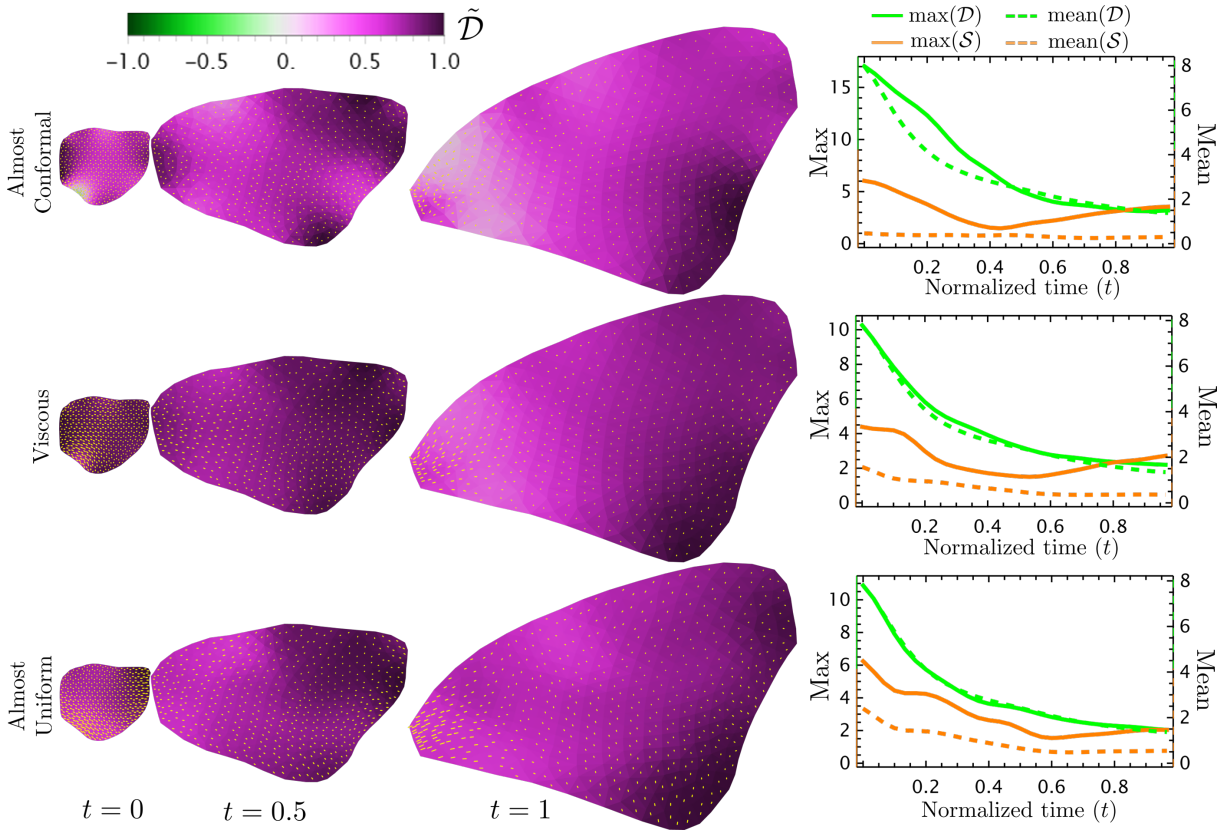

Figure S2: **Optimal 2D quasi-conformal flows for buckeye butterfly wings registration without landmarks.** Images of growing *Junonia coenia* (buckeye butterfly) wings are taken from [2] and processed as described in the main text. To infer the possible growth patterns, we run the optimization with three different parameter choices given in Table 2 in the main text: Almost-Conformal, Viscous, and Almost-Uniform (see the caption of main text Fig. 4 for details).

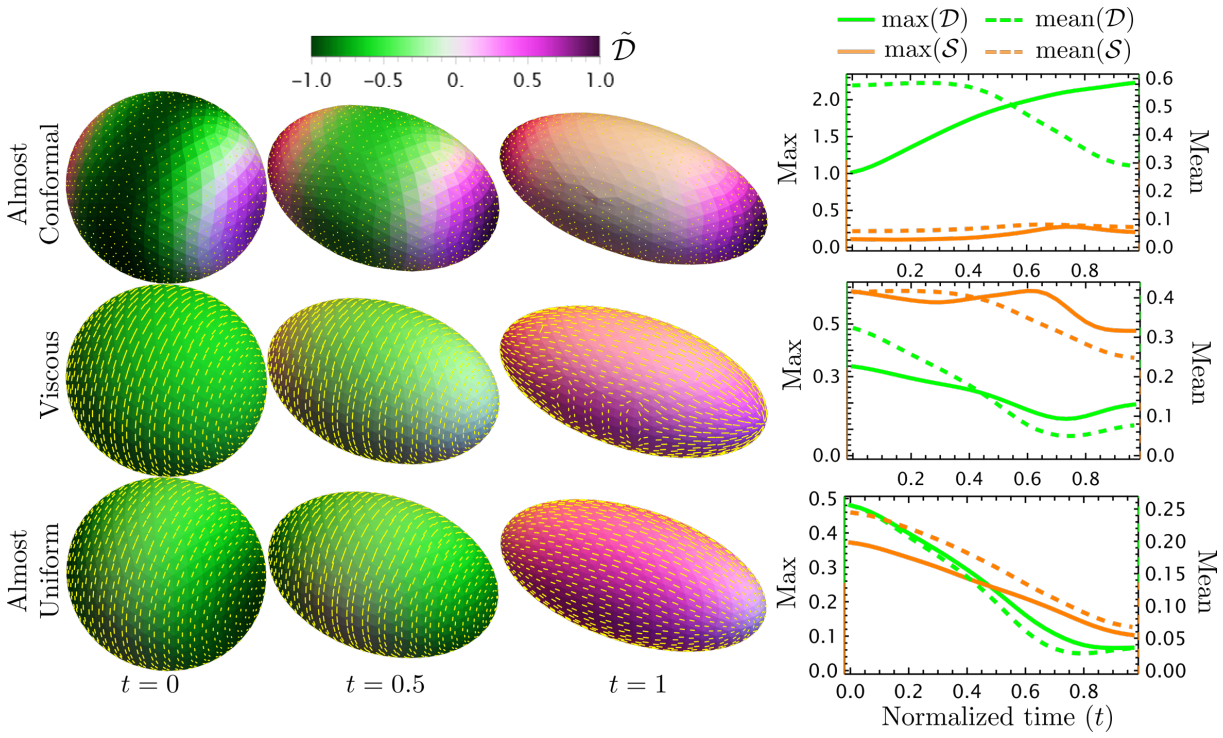

Figure S3: **Optimal 3D quasi-conformal flows for closed surface.** from a sphere deforms uniformly while conserving volume by expanding along one axis by a factor of 1.5 and contracting along the other two over the course of $T = 30$ time steps. To infer the possible growth patterns, we run the optimization with three different parameter choices given in Table 2 in the main text: Almost-Conformal, Viscous, and Almost-Uniform (see the caption of main text Fig. 4 for details).

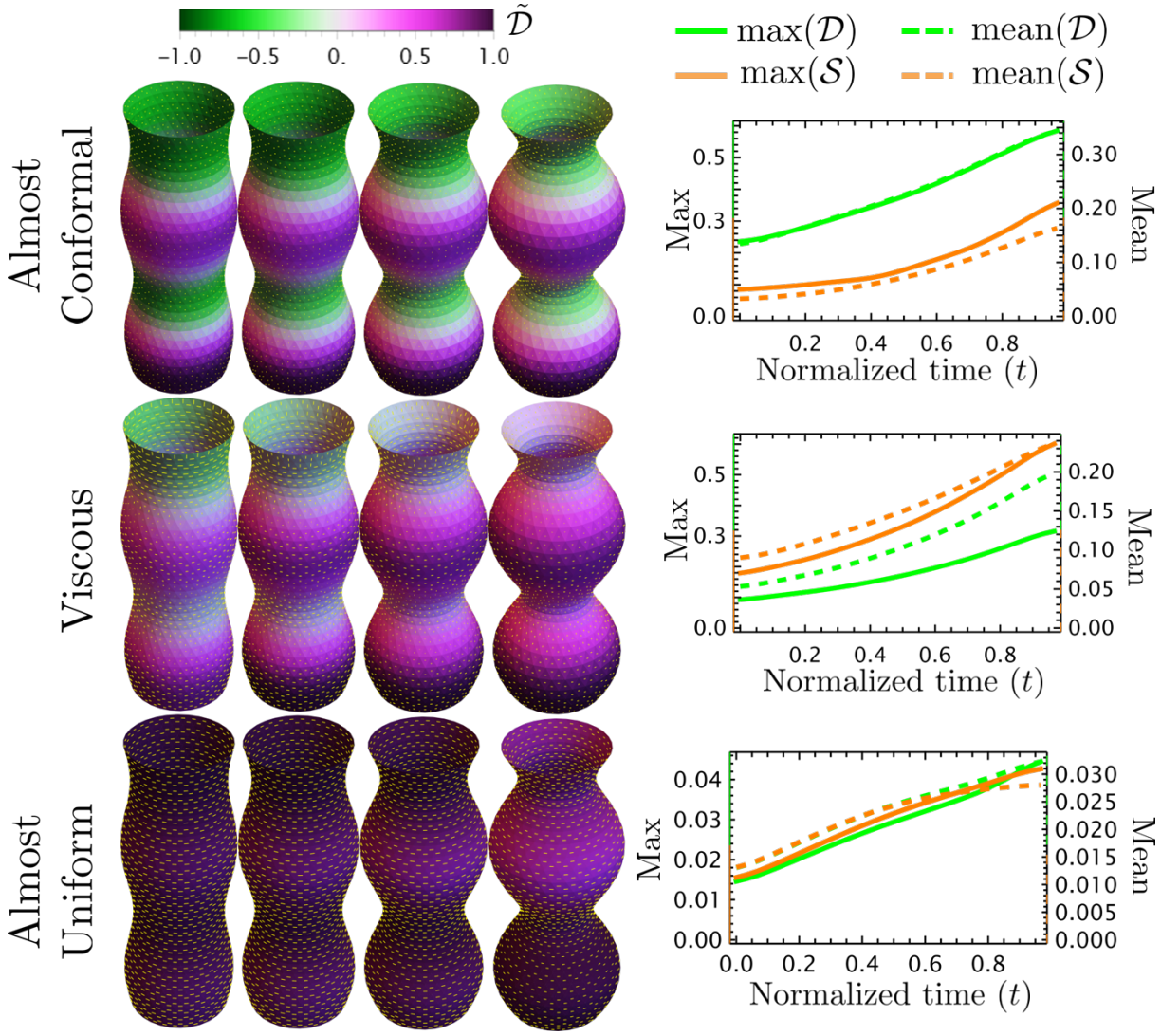

Figure S4: **Optimal 3D quasi-conformal flows for surfaces with boundary.** Results corresponding to the examples generated by Eq. (4.1) in the main text. To infer the possible growth patterns, we run the optimization with three different parameter choices given in Table 2 in the main text: Almost-Conformal, Viscous, and Almost-Uniform (see the caption of main text Fig. 4 for details).

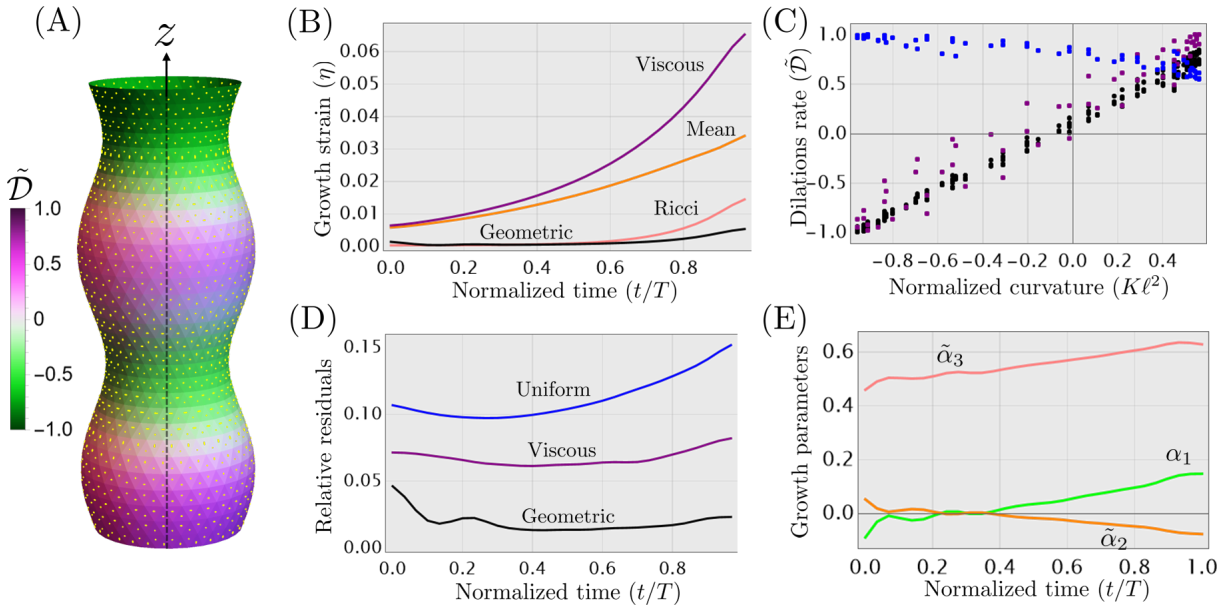

Figure S5: **Optimal 3D quasi-conformal flows using geometric flows.** Panel (A) shows a snapshot ($t/T = 0.5$) from the transformation shown in SI Fig. S4, where the registration is obtained by fitting to the nearest Ricci flow as described in the main text. Panel (B) compares the strain magnitude $\eta \equiv Tr[G_{ij}^2]$, where G_{ij} is defined in main text. The fit to the Ricci flow (pink), reduces the growth strain more than the mean curvature flow (orange). The fit to the combined flow (mean curvature and Ricci) is shown in black. Panel (C) shows the Gaussian curvature plotted against dilations, which are highly correlated when the registration is fit to the nearest Ricci flow (with Pearson coefficient of 0.998), unlike the uniform fit shown in red (with Pearson coefficient of 0.48). Panel (D) shows the mean absolute value of the residuals from the linear fit shown in Panel (C) for different registrations, normalised by $\Delta\mathcal{D} = \max(\tilde{\mathcal{D}}) - \min(\tilde{\mathcal{D}})$. Panel (E) gives the resulting parameters of the growth law obtained using the best fit to the combined flow, here $\tilde{\alpha}_2 \equiv \alpha_2 \mathcal{A}\bar{K}$ and $\tilde{\alpha}_3 \equiv \alpha_3 \mathcal{A}\bar{K}$, where $\bar{K}$ is the maximum value of the Gaussian curvature of the surface $\mathcal{X}_t$ and $\mathcal{A}$ is the area as before.

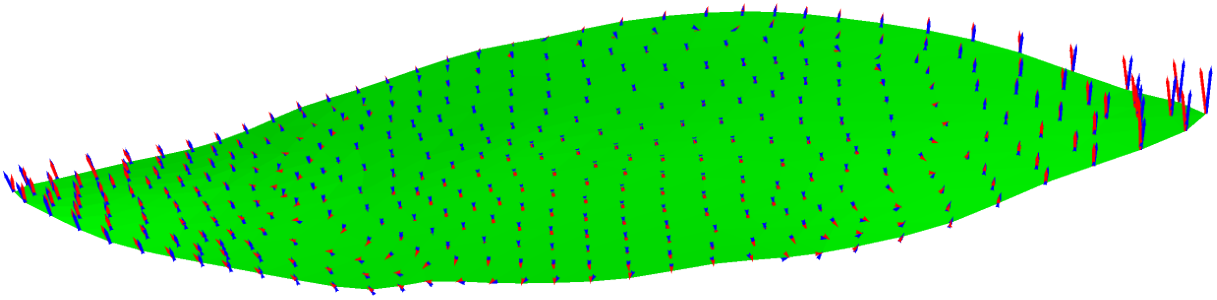

Figure S6: **Comparison of landmark and computed velocities.** This figure compares the leaf landmark velocity (red arrows), to the landmark velocity generated by the Ricci flow model at time step $N = 15$. To compare the computed and landmark velocities, we average their relative difference, $\epsilon_V \equiv |(\mathbf{V} - \mathbf{V}_L)/\mathbf{V}_L|$, across all vertices and all time steps. We find that ϵ_V is smallest for the Ricci flow and in particular the order is: Ricci ($\epsilon_V = 0.41$), Mean curvature ($\epsilon_V = 0.43$), Conformal ($\epsilon_V = 0.5$), Viscous ($\epsilon_V = 0.57$), and Uniform ($\epsilon_V = 0.57$).

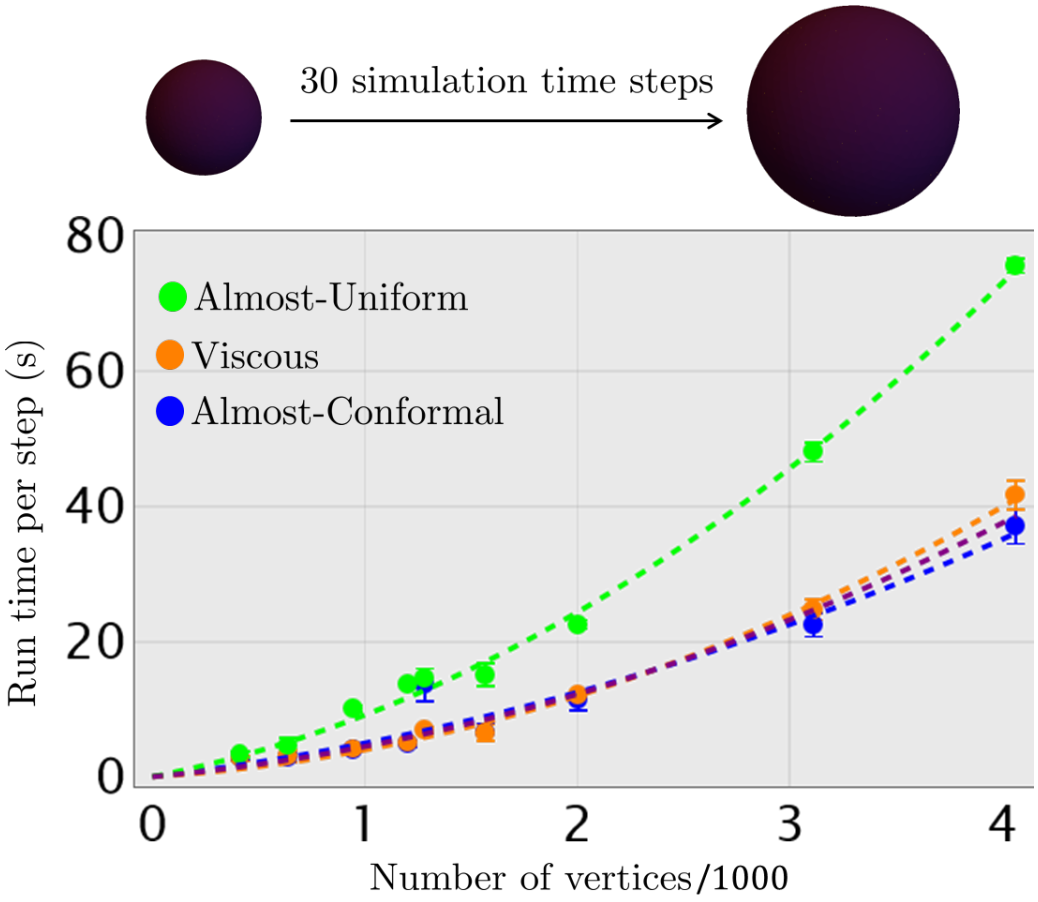

Figure S7: **Computational cost for different mesh sizes.** This figure quantifies the run time per simulation step ($N \to N+1$), in which the cost function is optimized for a uniformly expanding sphere and the David mesh example given in the main text, with the x-axis being the number of vertices divided by 1000 (n_V). The dashed lines show each model's quadratic fit (starting at the origin). Due to gradient cost computations, the Almost-Uniform model has higher computational cost (fit given by $\mathcal{T}_{step} = 6.1 n_V + 3.0 n_V^2$) than the Almost-Conformal and viscous models (average fit shown in purple, given by $\mathcal{T}_{step} = 2.8 n_V + 1.6 n_V^2$). Note that these times do not include the data preparation and preprocessing steps — done in Mathematica and Matlab as described in Section 3(a) of the main text.

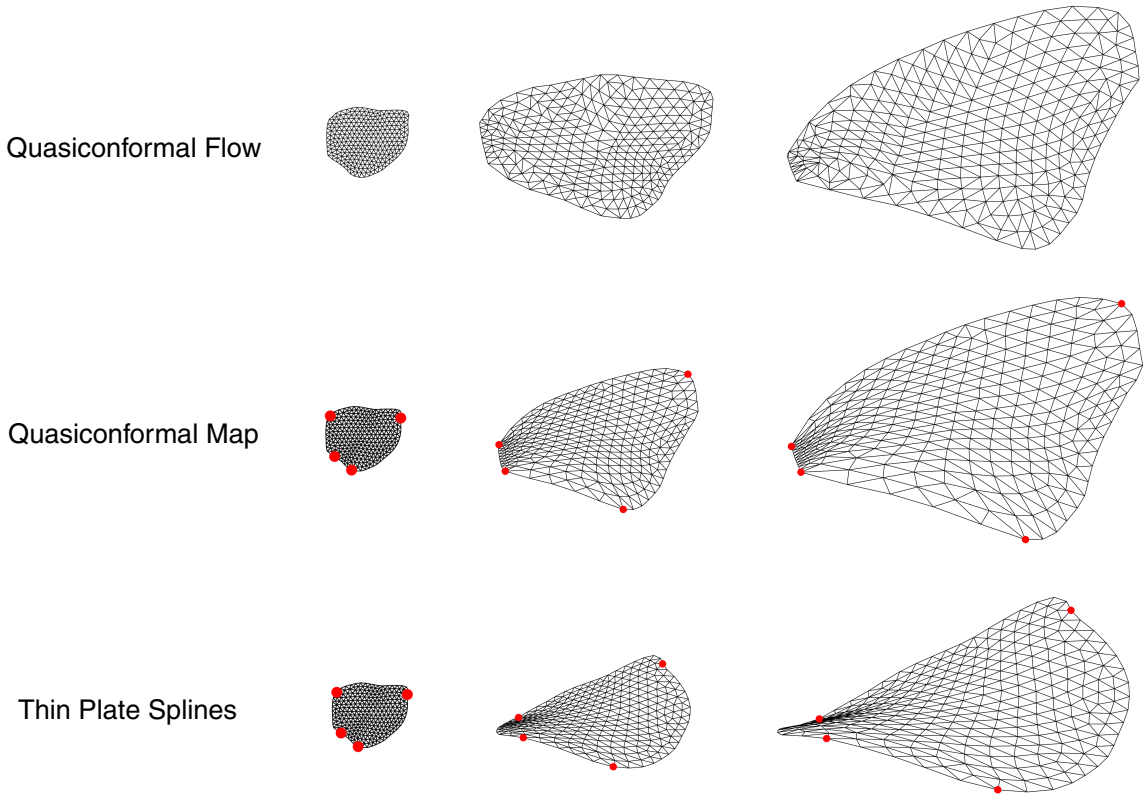

Figure S8: **Comparison between our quasi-conformal flow model and other mapping methods.** Here, we compare our quasi-conformal flow model with the quasi-conformal mapping method [3] and the Thin Plate Splines mapping method [4]. For the quasi-conformal flow model, the leftmost shows the initial time point, the middle shows the computation result at the intermediate time point, and the rightmost shows the final time point. Note that all intermediate states are taken into account in the computation for capturing the continuous growth process. On the contrary, both the quasi-conformal mapping method and the Thin Plate Splines mapping method rely only on the initial and final time points of the growth process. Specifically, the quasi-conformal mapping method computes a landmark-based registration between the initial and final time points with the prescribed landmarks (highlighted in red) and the boundary matched, while the Thin Plate Splines method only utilizes the prescribed landmarks in the initial and final time points to compute a deformation between the overall shapes. The intermediate state is then inferred using the mapping result. Comparing the overall shape of the intermediate states, it can be observed that the two mapping methods cannot recover the actual intermediate shape well. This shows the importance of using the proposed quasi-conformal flow method for studying the growth process of biological structures.